Development of Nanostructured Lipid Carriers for the Delivery of Idebenone in Autosomal Recessive Spastic Ataxia of Charlevoix-Saguenay

ACS OMEGA

http://pubs.acs.org/journal/acsodf

Article

Development of Nanostructured Lipid Carriers for the Delivery of Idebenone in Autosomal Recessive Spastic Ataxia of Charlevoix-Saguenay

Chiara Martinelli,* Matteo Battaglini, Carlotta Pucci, Sara Gioi, Chiara Caracci, Gaia Macaluso, Stefano Doccini, Filippo M. Santorelli, and Gianni Ciofani*

Cite This: *ACS Omega* 2020, 5, 12451−12466

Read Online

ACCESS | Metrics & More | Article Recommendations | Supporting Information

ABSTRACT: Oxidative stress occurs when physiological antioxidant systems do not manage to counteract the excessive intracellular production of reactive oxygen species (ROS), which accumulate leading to irreversible oxidation of DNA and other biomacromolecules, and thus to the onset of pathological conditions. Autosomal recessive spastic ataxia of Charlevoix-Saguenay (ARSACS) is a neurodegenerative disease characterized by autosomal recessive mutations in the sacsin gene (*SACS*). It has been demonstrated that cells of ARSACS patients show bioenergetic and mitochondrial impairment, denoted by reduced respiratory chain activities and ATP synthesis. In order to design a suitable therapy for ARSACS, it is essential to consider that treatments need to cross the blood−brain barrier (BBB), a specialized structure that separates the subtle environment of the brain from blood circulation. Nanostructured lipid carriers (NLCs), constituted by a solid lipid shell and a liquid lipid phase in the core, have been fabricated for loading hydrophobic molecules, improving their bioavailability. Idebenone (IDE), a synthetic analogue of coenzyme Q_{10}, is able to inhibit lipid peroxidation and detoxify several free radicals. However, because of its poor solubility, it requires *ad hoc* drug-delivery systems for enhancing its pharmacokinetic properties, preventing undesired cytotoxicity. In this work, NLCs loaded with idebenone (IDE-NLCs) have been prepared. The nanovectors have been physicochemically characterized, and their biological activity has been evaluated on different central nervous system cell lines. IDE-NLCs demonstrated to be stable in water and in cell culture media, and showed a sustained drug release profile. Interestingly, preliminary data demonstrated their ability to permeate an *in vitro* BBB model. Their protective antioxidant activity in human healthy primary skin fibroblasts and their therapeutic efficacy in ARSACS-derived primary skin fibroblasts have been also investigated, showing their potential for future development as therapeutic agents.

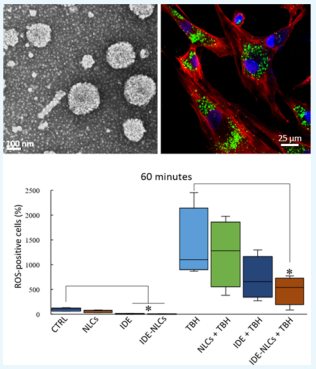

INTRODUCTION

Neurodegenerative diseases (NDs) are a group of pathologies involving the central nervous system, primarily affecting neurons and characterized by common features and symptoms. They are mainly irreversible and may arise from genetic mutations, endogenous issues, or environmental factors.[1] Moreover, it is well known that misfolding of specific proteins, oxidative injury, and mitochondrial dysfunctions are responsible for the disruption of neuronal and axonal transports, and consequent apoptotic phenomena.[1] It has been demonstrated that cells involved in these pathologies display higher production of reactive oxygen species (ROS) with respect to their healthy counterparts.[2] Accumulation of ROS induces oxidation of biological substrates and oxidative stress. This phenomenon is emphasized by the abnormal functioning of the mitochondria, where ATP production and calcium regulation normally take place. Many neuronal groups require high demands of ATP for axonal transport, and when combined with mitochondrial impairment, they result in being more sensitive to degeneration.[3] High levels of oxidative stress favor mitochondrial permeability transition, responsible for threatening ionic homeostasis of neurons, altering their metabolism, and contributing to cytotoxicity and necrosis/apoptosis.[1,4]

Autosomal recessive spastic ataxia of the Charlevoix-Saguenay type (ARSACS: MIM 270550) is an noncurable, childhood-onset ND, characterized by autosomal recessive mutations in *SACS* gene, encoding sacsin,[5] a protein expressed on the mitochondrial surface and involved in abnormal bundling of neurofilaments of neuronal cells and in mitochondrial network organization.[6] Patients harboring biallelic variants in *SACS* present progressive cerebellar atrophy and damage of the peripheral nerves,[7] and they also manifest significant retinal changes and cognitive impairment.[8]

Received: March 23, 2020
Accepted: May 7, 2020
Published: May 14, 2020

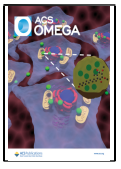

Although the functional role of sacsin and the pathophysiological consequences of its dysfunction have not been fully understood, it is known that ARSACS cells show bio-energetic and mitochondrial damage, denoted by reduced respiratory chain activities and ATP synthesis.[6] Sacsin has been revealed to play a role in the correct localization of the mitochondria in neurons and in normal dendritic morphology.[7] It has been demonstrated that sacsin knockdown leads to a more interconnected mitochondrial network and to a change in the mitochondria morphology toward a "balloon-like" shape.[7] The hyperfused mitochondrial phenotype and lack of fission seem to confirm that sacsin is essential in determining their shape. Consequently, it has been hypothesized that loss of sacsin alters correct neuronal development, growth, and synaptic function.[9,10]

No effective therapies have been proposed for ARSACS. To design a suitable treatment for patients, it is essential to consider that potential drugs need to cross the blood−brain barrier (BBB), an ultra-specialized structure that separates the subtle environment of the brain from blood circulation. Indeed, because of its physical features, such as lack of fenestrations and a very low rate of pinocytosis, the passage of the vast majority of therapeutic molecules and drugs is blocked.[11] To overcome BBB crossing difficulties, biocompatible nanovectors have been developed, that are recognized by brain cells, easily transportable in the bloodstream, and carrying drugs for targeted delivery.[4]

Innovative fabrication techniques based on the use of natural lipids, which facilitate encapsulation of hydrophobic drugs preventing their degradation and decreasing systemic side effects, easy to be functionalized for active targeting, and allowing controlled drug release, have been recently introduced.[12] Nanostructured lipid carriers (NLCs) are constituted by a solid lipid structure including a liquid lipid phase in the core. This feature makes their structure less crystalline with respect to solid lipid nanoparticles (SLNs), increasing the amount of loadable payload and improving drug availability.[13]

Idebenone (IDE) is a synthetic analog of coenzyme Q_{10} (CoQ_{10}).[14] Some evidences demonstrate that IDE inhibits lipid peroxidation and detoxifies several free radicals.[15] IDE is employed in the treatment of diseases with mitochondrial etiology, and it has been investigated for the treatment of Friedreich's ataxia (FA), a progressive inherited ataxia.[16] IDE (Raxone) has been approved by the European Medicine Agency to treat visual impairment in adolescents and adults.[17,18] Despite the fact that IDE is less lipophilic than CoQ_{10}, it still remains poorly water-soluble; therefore, *ad hoc* drug-delivery systems have been designed to improve its pharmacokinetics, physicochemical properties, and stability, preventing undesired cytotoxicity.[19]

Several studies have been performed to investigate the effect of IDE-loaded liposomes on cell viability, as compared to the free drug. Two research groups encapsulated IDE in conventional liposomes and PEGylated large unilamellar vesicles.[20,21] These nanocarriers showed improved bioavailability and reduced ethanol-induced damages upon administration. However, liposomal formulations displayed some stability issues and fast clearance problems. Stancampiano *et al.* proposed the *quasi*-emulsion solvent diffusion method to encapsulate IDE in SLNs. They showed how IDE-loaded SLNs displayed efficient antioxidant activity upon stress induced by thermolysis of 2,2-azobis 2-amidopropane dihydrochloride (APPH) and lower induced release of lactate dehydrogenase (LDH) in primary cultures of astrocytes, as compared to free IDE.[22] However, because of lipid peroxidation, SLNs caused increased oxidative stress directly proportional to their concentration. Modifying the preparation procedure, Montenegro *et al.* demonstrated an improved ROS inhibition in primary cultures of astrocytes.[23] Permeability experiments on an *in vitro* model of BBB were successfully performed.[24]

In this work, NLCs loaded with IDE (IDE-NLCs) have been prepared for improving its delivery and intracellular release. Nanovectors encapsulating IDE have been physicochemically characterized, and their biological activity has been evaluated in terms of cytotoxicity in different central nervous system cell lines. IDE-NLCs demonstrated to be stable in water and in cell culture media at different pH conditions and showed a sustained release profile up to 72 h. Preliminary experiments demonstrated their ability to permeate an *in vitro* BBB model. Their protective antioxidant activity on human healthy primary skin fibroblasts and their therapeutic efficacy in ARSACS-derived primary skin fibroblasts has also been investigated. The aim of this research is to provide a novel nanosystem able to counteract the high levels of oxidative stress caused by excessive ROS production in ARSACS patients, contributing to the reduction of the symptoms associated with this pathology.

MATERIALS AND METHODS

Preparation and Purification. NLCs were fabricated by high-temperature homogenization. The liquid lipid component, 2.5 mg of oleic acid (Sigma-Aldrich), and the solid lipid component, 27.5 mg of cetyl palmitate (Gattefossé SAS), were mixed to 4 mg of mPEG-DSPE (5000 Da; Nanocs Inc.) at 70 °C (over their melting temperature) to allow the rapid evaporation of ethanol (used as the solvent; Sigma-Aldrich). These materials have been chosen for their high biocompatibility and being previously reported for NLC preparation.[25] The lipid components were mixed with 1 mg of IDE (Sigma-Aldrich) dissolved in 100 μL of ethanol for preparing IDE-NLCs. Plain NLCs were prepared as control by mixing lipid components with 100 μL of ethanol. Pluronic F-127 (Sigma-Aldrich) at 10 mg/mL in water was added as a stabilizer (3 mL), and the emulsion was finally vortexed for 1 min and sonicated (Thermo Fisher−Fisher Scientific FB120) for 10 min at 90% amplitude and stored at 4 °C for 30 min. NLCs were then purified using Amicon Ultra-4 Centrifugal Filter Units (MWCO 100 kDa; Sigma-Aldrich) by centrifuging at 8230 rpm for 40 min at 4 °C three times. The filtered pellet was resuspended in sterile water, and the final suspension was finally filtered using a 1.2 μm syringe filter and a 0.2 μm sterile syringe filter (Sartorius Minisart Plus Syringe Filters) under a biological hood. The concentration of IDE-NLCs was determined using freeze-dried samples known amounts of the final dispersion. For nanoparticle/cell interaction studies, IDE-NLCs were labeled with Vybrant DiO cell-labeling solution (Thermo Fisher). Particles (200 μL) were incubated for 1 h at 37 °C with 5 μM dye. Successively, they were washed three times with Amicon Ultra-4 Centrifugal Filter Units (MWCO 100 kDa; Sigma-Aldrich). The collected final pellet was resuspended in 200 μL of distilled sterile water.

Dynamic Light Scattering Measurement. Dynamic light scattering (DLS; Malvern-Zetasizer Nano ZS90) measurements were performed in order to evaluate size, polydispersity index (PDI), and ζ-potential of IDE-NLCs. Disposable polystyrene cuvettes (Malvern Zetasizer Nano series) were used to measure IDE-NLC average hydrodynamic

https://dx.doi.org/10.1021/acsomega.0c01282
ACS Omega 2020, 5, 12451−12466

diameter, while disposable folded capillary cells (Malvern Zetasizer Nano series) were used to measure ζ-potential. The temperature was set at 25 °C and the equilibration time at 120 s. In order to assess the long-term stability of IDE-NLCs, size and PDI measurements were performed by diluting nanoparticles in water, phosphate-buffered saline (PBS), Dulbecco's modified Eagle medium (DMEM), and DMEM supplemented with 10% fetal bovine serum (FBS). Measurements have been performed upon 24, 48, 72, 168, 336, 504, and 720 h of incubation at 37 °C.

Transmission Electron Microscopy. High-resolution transmission electron microscopy (TEM) was performed to evaluate IDE-NLCs morphology. Samples were diluted and sonicated for 5 min. A drop of the sample solution was placed on a Cu grid, 150 mesh, coated with ultrathin amorphous carbon film, previously plasma-treated (O^{2+}Ar plasma, 10 W, 2 min), to remove hydrocarbon residues from carbon film deposition. The grids were stored in air. The staining procedure, to enhance the contrast of lipid particles, consisted of a 30 s treatment of previously prepared sample grids with 1% uranyl acetate solution in water.

Drug Loading and Release. Samples were analyzed by high-performance liquid chromatography (HPLC; Shimadzu LC-20AT), with an Agilent TC C18 (150 mm × 4.6 mm—particle size of 5 μm, pore size of 170 Å) chromatographic column and a UV detector. The mobile phase was composed of 100% acetonitrile (for HPLC, ≥ 99.9 %, Sigma-Aldrich), pumped in isocratic mode at a flow rate of 1 mL/min. The absorbance peak of IDE was detected at 276 nm. IDE-NLCs (200 μL) were frozen at −80 °C and subsequently freeze-dried overnight. Acetonitrile (300 μL) was added to each sample and left on a hot plate at 70 °C for 1 h. Cold sterile water (200 μL) was added, and samples were centrifuged for 1 h at 15,000 rpm at 4 °C, allowing the lipids to precipitate. Once collected, the supernatant was analyzed by HPLC. A calibration curve was obtained by dissolving pure IDE in acetonitrile. Drug loading was calculated according to the following equation

$$\text{drug loading (\%)} = \frac{\text{idebenone mass in NLCs (mg)}}{\text{total mass of NLCs (mg)}} \times 100 \quad (1)$$

Release studies were performed by dispersing IDE-NLCs in different buffers. IDE-NLCs (2 mg) were diluted into PBS (phosphate-buffered saline solution, without Ca^{2+} and Mg^{2+}; Sigma-Aldrich) at pH 7.4, in PBS pH 7.4 with 100 μM H_2O_2, in 0.05 M phosphate buffer solution (potassium dihydrogen phosphate) pH 4.5, or in 0.05 M phosphate buffer solution pH 4.5 with 100 μM H_2O_2. Samples were maintained at 37 °C under agitation, and the concentrations of drug released were evaluated at 4, 8, 24, and 72 h after filtration with Amicon Ultra-4 Centrifugal Filter Unit (MWCO 100 kDa; Sigma-Aldrich) at 8230 rpm for 40 min at 20 °C. Supernatants were analyzed by HPLC. After the acquisition, the cumulative percentage release was calculated.

Cell Cultures. Mouse astrocyte cells C8-D1A (ATCC CRL-2541), mouse brain endothelial cells bEnd.3 (ATCC CRL-2299), and human healthy and ARSACS patient's primary fibroblasts derived from skin punch biopsies were cultured in DMEM high glucose (Sigma-Aldrich) supplemented with 10% heat-inactivated FBS (Gibco), 2 mM L-glutamine (Gibco), 1 mM sodium pyruvate (Gibco), 100 IU/mL of penicillin, and 100 μg/mL of streptomycin (all from Gibco). Human fibroblasts were collected with informed consent according to standard procedures for diagnostic skin biopsies and treated according to the standards of good clinical practice. Primary skin fibroblasts derived from two healthy controls and two ARSACS patients at similar culture passages (P5−P15) were investigated.

Human neuroblastoma cells SH-SY5Y (ATCC CRL-2266) were cultured in a 1:1 mixture of DMEM and Ham's F-12 nutrient mixture (Sigma-Aldrich), supplemented with 10% heat-inactivated FBS (Gibco), 2 mM L-glutamine (Gibco), 1 mM sodium pyruvate (Gibco), 100 IU/mL of penicillin, and 100 μg/mL of streptomycin (all from Gibco). Cells were induced to differentiate in human neuron-like cells by serum deprivation (1% FBS; Gibco) and retinoic acid addition (10 μM; Sigma-Aldrich).[26]

Biocompatibility Investigation. For WST-1 assay, cells were seeded in a 24-well cell culture plates (COSTAR) at a density of 1.5×10^4 cells/well. After 24 h, cells were incubated with IDE-NLC preparations at different IDE molar concentrations in complete DMEM without phenol red (Sigma-Aldrich). In parallel, cells were incubated with free IDE dissolved in ethanol and NLCs. Studies were performed at 24 and 72 h after incubation at 37 °C, 5% CO_2. Dilution (1:20) of cell proliferation reagent WST-1 (Roche) was prepared in 300 μL/well of DMEM without phenol red, and plates were incubated at 37 °C for 30 min. Absorbance reading was performed with a Victor X3 Multilabel Plate Reader (Perkin Elmer), setting absorbance wavelength at 450 nm and 0.1 s measurement time. Cells were then rinsed with PBS and frozen at −80 °C. Frozen samples were treated to assess the proliferation rate by Quant-iT PicoGreen dsDNA Assay Kit (Invitrogen). Samples stocked at −80 °C were subjected to three cycles of freeze/thaw in order to allow cell lysis and DNA release. Meanwhile, a series of dilutions of the reagent and buffer were prepared according to the manufacturer's instructions. Fluorescence was measured with Victor X3 Multilabel Plate Reader (Perkin Elmer), setting the excitation wavelength at 485 nm, emission wavelength at 535 nm, and 0.1 s measurement time.

Nanoparticle/Cell Interactions. Cells were seeded in μ-plate 24-well black IbiTreat (Ibidi) at a density of 2×10^4 cells/well. After 24 h, they were incubated with 300 μg/mL of Vybrant DiO-labeled IDE-NLCs at 37 °C. At 24 and 72 h after incubation, they were rinsed with PBS and fixed with 4% paraformaldehyde at 4 °C for 30 min. After rinsing with PBS, staining was performed by incubating cells with Hoechst 33342 dye (1 mg/mL, diluted 1:1000; Thermo Scientific) and TRITC-phalloidin (2.5 μg/mL; Sigma-Aldrich) in 10% goat serum (Euroclone) for 90 min at 37 °C. After a final rinse with PBS, 500 μL of PBS were added and plates were stored at 4 °C in the dark. A C2s confocal laser scanning microscopy (CLSM) system, employing NIS-Elements software (Nikon), was used for 2D and 3D confocal acquisitions.

A total of 2×10^4 cells/well was seeded in 24-well cell culture plates (COSTAR). After 24 h, they were incubated with 300 μg/mL of Vybrant DiO-labeled IDE-NLCs in complete DMEM without phenol red (Sigma-Aldrich). Samples were analyzed at 24, 48, and 72 h. Cells were collected and centrifuged at 2600 rpm for 6 min. The pellet was resuspended and transferred in Cytoflex Tubes (Bio-Rad). FITC events were acquired using a flow cytometer (Cytoflex, Beckman Coulter). The measurement threshold was set to 10^4 events/sample.

https://dx.doi.org/10.1021/acsomega.0c01282
ACS Omega 2020, 5, 12451−12466

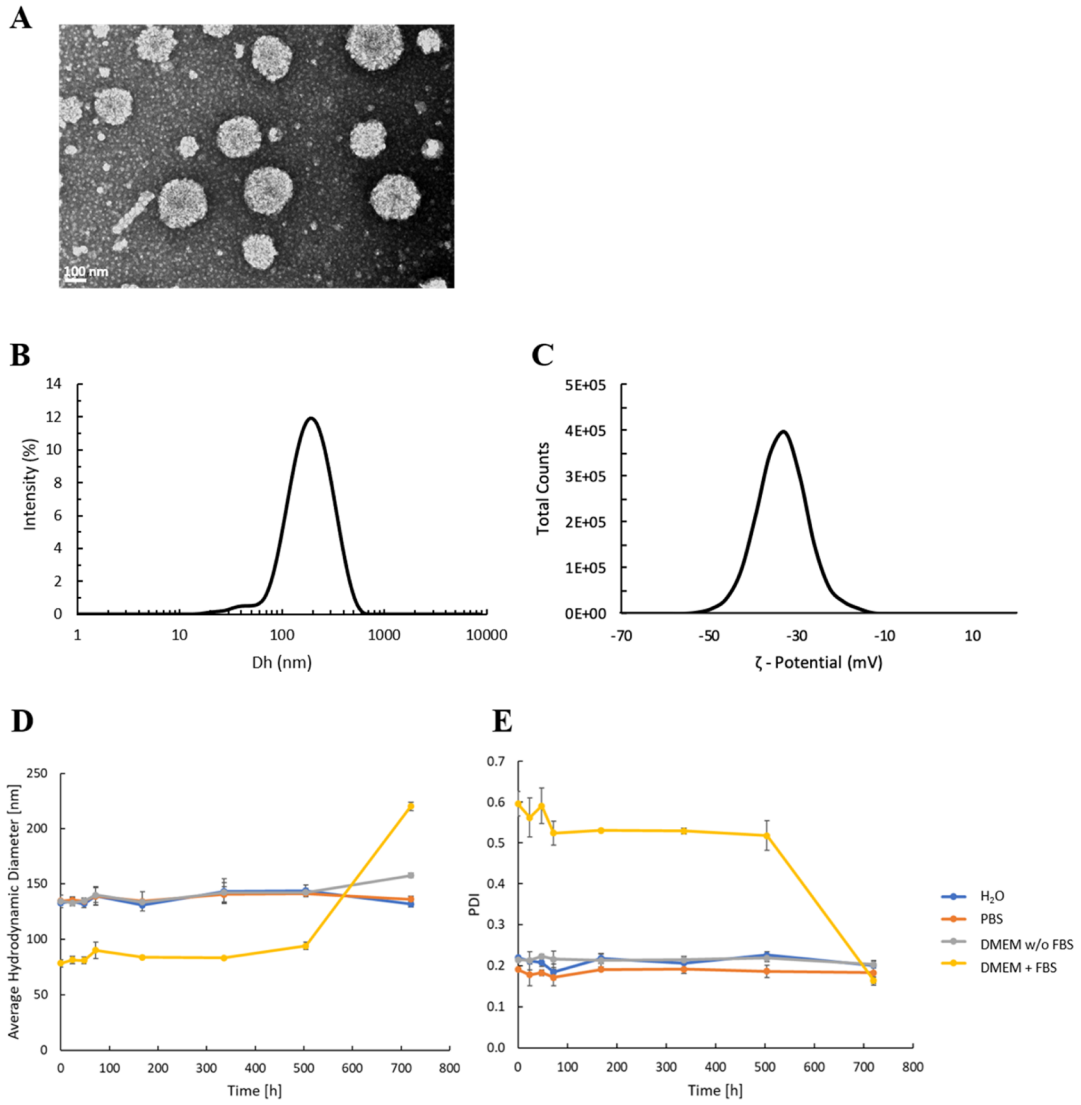

Figure 1. (A) Representative TEM image of IDE-NLCs. (B) Size measurement of IDE-NLCs performed by DLS. (C) ζ-potential measurement of IDE-NLCs. (D) Average hydrodynamic diameter measurement of IDE-NLCs performed by DLS. (E) PDI measurement of IDE-NLCs performed by DLS. Stability measurements were performed in water, PBS, DMEM, and DMEM supplemented with 10% FBS at 37 °C.

Blood–Brain Barrier *In Vitro* Model. To set up the model to assess the ability of developed nanovectors to cross the barrier, a two-compartment system consisting of porous scaffolds (24-well transwell inserts with pore size of 3.0 μm diameter PET track-etched membrane; Corning) was used to culture brain endothelial cells (bEnd.3) and astrocytes (C8-D1A) at high confluence. The two cell lines were cultured on opposite sides of the porous scaffold which separates the luminal chamber (on the upper part) from the abluminal compartment (on the lower part). C8-D1A cells were seeded on the bottom side of the porous membrane, with a cell density of 1×10^4 cells/cm^2. After 24 h, the inserts were flipped back up, and bEnd.3 cells were seeded on the apical side of the membrane at 3×10^4 cells/cm.[2] The luminal compartment (top) was filled with 200 μL of complete DMEM without phenol red, while the abluminal chamber (bottom) was filled with 700 μL of complete DMEM without phenol red. Cells were kept at 37 °C, 5% CO_2, for five days.

The system was then characterized and exploited for permeability studies. Bioelectrical properties of the cell bilayer (C8-D1A and bEnd.3) were checked by measuring the transendothelial electrical resistance (TEER), assessed with a Millipore Millicell ERS-2 Volt-Ohmmeter. BBB integrity was verified by measuring the permeability of FITC-dextran (70 kDa; Sigma-Aldrich) at different time points. A calibration curve was obtained by dissolving FITC-dextran in complete DMEM without phenol red. Samples were measured with Victor X3 Multilabel Plate Reader (Perkin Elmer), setting the excitation wavelength at 485 nm and emission wavelength at 535 nm, 0.1 s measurement time. Fresh medium (700 μL) was added on the barrier abluminal compartments, and 200 μL of 200 μg/mL diluted of FITC-dextran solution was added in the barrier luminal compartments (on top). Membranes without cells were analyzed as a control in the same conditions. Analyses were conducted by measuring fluorescence of medium recovered in the abluminal space at 1, 4, 8, 24, 48, and 72 h. Subsequently, IDE-NLC permeation experiments were conducted. The calibration curve was performed for Vybrant DiO-labeled IDE-NLCs in complete DMEM without phenol red. Samples were measured with Victor X3 Multilabel Plate Reader (Perkin Elmer), setting the excitation wavelength at 485 nm, emission wavelength at 535 nm, and 1.0 s

https://dx.doi.org/10.1021/acsomega.0c01282
ACS Omega 2020, 5, 12451−12466

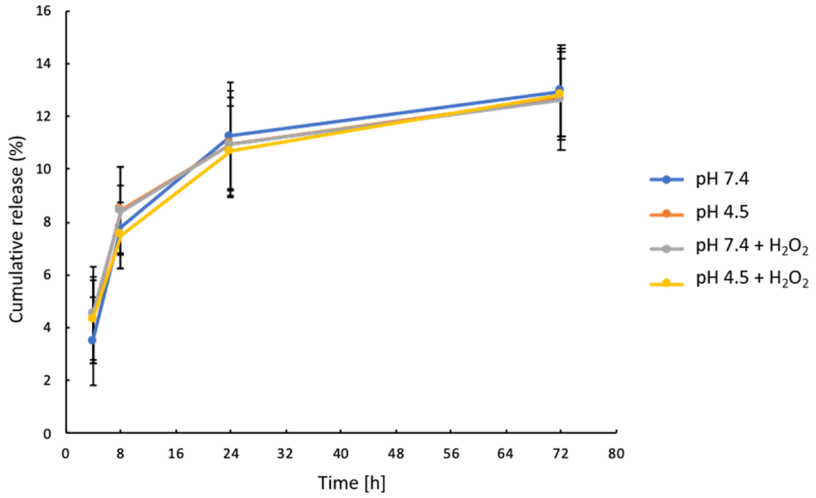

Figure 2. Cumulative release profile of IDE-NLCs in different buffers. Measurements were performed at pH 7.4, pH 4.5, pH 7.4 + H_2O_2, pH 4.5 + H_2O_2.

measurement time. Fresh medium (700 μL) was added on the barrier abluminal compartments, and 200 μL of 500 μg/mL Vybrant DiO-labeled IDE-NLC dispersion was added in the barrier luminal compartments. Analyses were conducted by measuring the fluorescence of medium recovered in the abluminal space at 1, 4, 8, 24, 48, and 72 h. 3D confocal images of the in vitro BBB model were acquired after 72 h of incubation with Vybrant DiO-labeled IDE-NLCs.

Evaluation of Antioxidant Activity. The antioxidant activity of IDE-NLCs was evaluated by flow cytometry in order to detect cell oxidative stress through a fluorogenic probe that enhances fluorescence upon ROS production. Cells were seeded in a 6-well cell culture cluster COSTAR at a density of 6×10^4 cells/well. After 24 h, they were incubated in complete DMEM without phenol red (Sigma-Aldrich) with IDE-NLCs, free IDE, (corresponding to the concentration encapsulated in 300 μg/mL of IDE-NLCs), and plain NLCs. Studies were performed after 72 h of incubation at 37 °C, 5% CO_2. The CellRox Green Reagent (Invitrogen) was diluted to a final concentration of 5 μM in complete medium without phenol red. Cells were rinsed once in PBS, and the reagent was added; after 30 min at 37 °C, cells were trypsinized for 5 min at 37 °C, collected, and centrifuged at 2600 rpm for 6 min. After medium removal, the pellet was resuspended in 1 mL of PBS and aliquoted into two Cytoflex Tubes (Bio-Rad), 500 μL each. Concerning healthy fibroblasts, one tube was kept as the control and the second one was treated by addition of 2.5 mM *tert*-butyl hydroperoxide (TBH; Sigma-Aldrich). Data were acquired using a flow cytometer (Cytoflex, Beckman Coulter). The measurement threshold was set to 10^4 events/sample. Two time points were considered, 30 and 60 min, after oxidative stress induction. The percentages of ROS-positive cells in each condition were normalized by the average of ROS-positive cells of the corresponding controls (healthy cells at 30 min, healthy cells at 60 min, patient's cells at 30 min and patient's cells at 60 min) derived from at least three independent experiments.

Statistical Analysis. Statistical analysis was performed using the *R* software. Normality of the data was checked through the Shapiro–Wilk test, normally distributed data were analyzed with the ANOVA test followed by the LSD *post-hoc* test with Bonferroni correction and expressed as mean ± standard deviation. Non-normally distributed data were analyzed with the Kruskal–Wallis test followed by the pairwise-Wilcoxon *post-hoc* test and expressed as median ± confidence interval.

RESULTS

Preparation and Physicochemical Characterization of IDE-NLCs. Upon fabrication of IDE-NLCs, nanovectors were stained for TEM imaging, in order to evaluate their morphology and size. Nanoparticles displayed good homogeneity (Figure 1A) and a size of approximately 150 nm. DLS measurement was performed to evaluate IDE-NLCs colloidal properties, such as size, PDI, and ζ-potential. The average hydrodynamic diameter was 159.3 ± 3.4 nm, with a PDI of 0.224 ± 0.015, indicating monodisperse preparations. Figure 1B reports the intensity distribution of the homogeneous IDE-NLCs population obtained by CONTIN analysis. The ζ-potential resulted to be −33.5 ± 0.1 mV (Figure 1C). This negative value is compatible with nanoparticle repulsion and low aggregation. In order to assess the long-term stability of the nanovectors, size (Figure 1D) and PDI (Figure 1E) measurements were conducted upon dilution of IDE-NLCs in different dispersants: water, PBS, DMEM, and DMEM supplemented with 10% FBS. Preparations were incubated at 37 °C and analyzed at different time points: 24, 48, 72, 168, 336, 504, and 720 h. Results demonstrated that IDE-NLCs show good stability at 37 °C, even after one month, and upon dilution in all the considered solvents.

Loading and Release Studies. In order to estimate the drug loading, lipids were dissolved and supernatants containing the encapsulated molecule were collected and measured by HPLC. IDE loading resulted to be 1.1 ± 0.4% w/w. After drug-loading quantification, release studies were performed. IDE-NLCs were diluted in different buffers, with variable pH, corresponding to physiological conditions (pH 7.4) and mimicking the intracellular acidic environment present in lysosomes (pH 4.5), with and without oxidative stress (100 μM H_2O_2). The profiles obtained by HPLC showed a sustained release up to 13 ± 2%, reaching a plateau after 72 h at 37 °C. No burst release was visible. It should be noted that the release was pH- and H_2O_2-independent (Figure 2).

https://dx.doi.org/10.1021/acsomega.0c01282
ACS Omega 2020, 5, 12451−12466

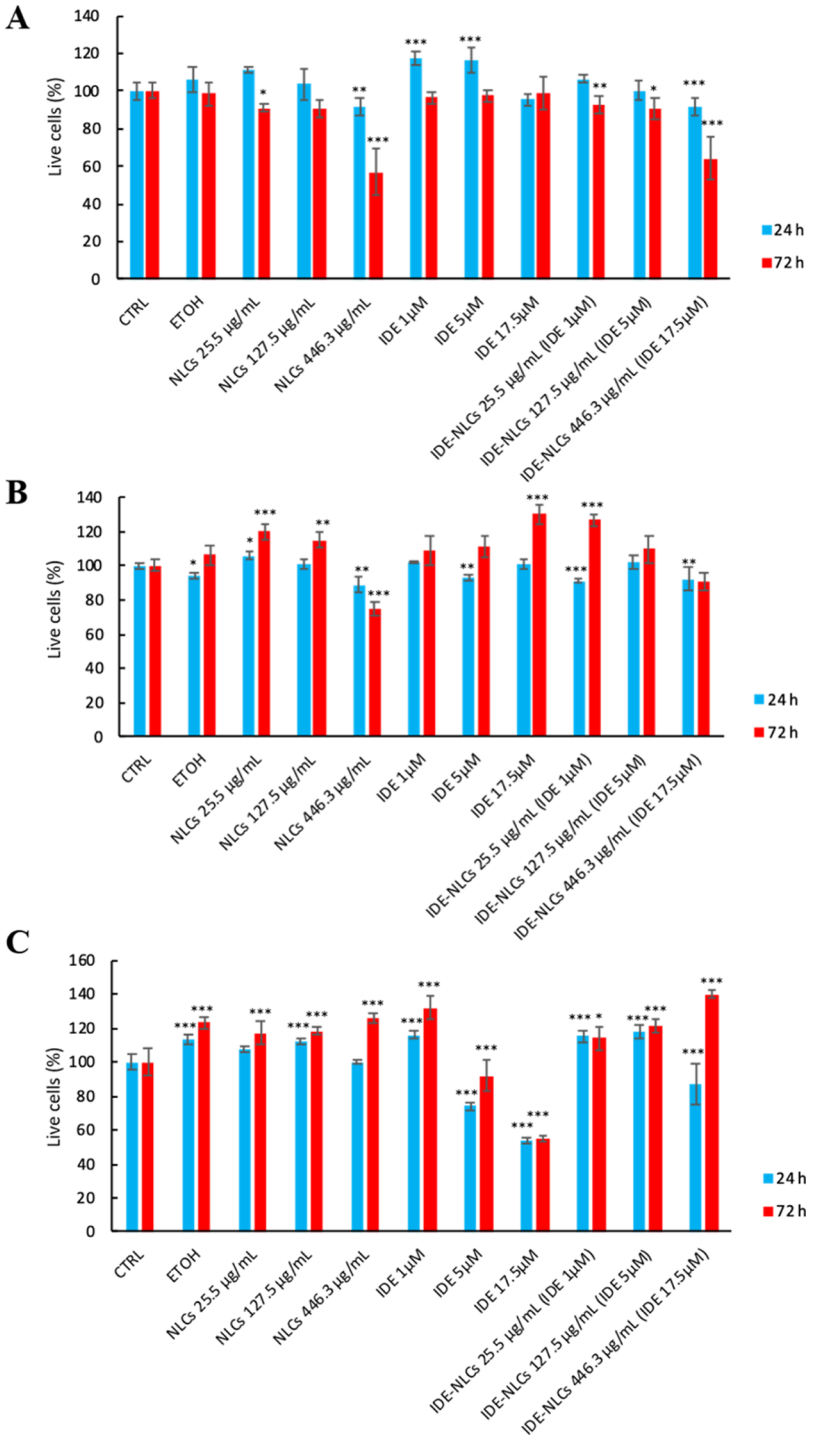

Figure 3. (A) WST-1 assay performed on C8-D1A astrocytes incubated with free IDE, IDE-NLCs, and NLCs. (B) WST-1 assay performed on bEnd.3 endothelial cells incubated with free IDE, IDE-NLCs, and NLCs. (C) WST-1 assay performed on differentiated SH-SY5Y neuron-like cells incubated with free IDE, IDE-NLCs, and NLCs. Analyses were normalized on nontreated cells (CTRL); cells were also treated with ethanol (ETOH, used for dissolving free idebenone). *p < 0.05, **p < 0.01, ***p < 0.001.

Evaluation of IDE-NLCs Cytotoxicity on Astrocytes, Endothelial, and Differentiated Neuron-like Cells. Evaluation of cytotoxicity was performed *in vitro* on different cell lines upon incubation with IDE-NLCs for 24, 48, and 72 h. C8-D1A mouse astrocytes, bEnd.3 mouse brain endothelial cells, and human differentiated SH-SY5Y neuron-like cells were chosen as they properly represent an *in vitro* model of the BBB functionality.[27] The cytotoxicity of IDE-NLCs was evaluated by WST-1 and PicoGreen assays that were performed in order to assess metabolic activity and proliferation rates of these cell lines at 24 and 72 h after administration of nanoparticles. Three IDE-NLCs concentrations were tested for each treatment: 25.5, 127.5, and 446.3 μg/mL corresponding to 1, 5, and 17.5 μM of the loaded drug. The highest concentration of IDE used in this work has been previously reported in a study exploiting IDE-loaded SLNs,[23] while the intermediate and lower ones were chosen in order to evaluate a possible range of cytotoxicity. In parallel, experiments were performed

https://dx.doi.org/10.1021/acsomega.0c01282
ACS Omega 2020, 5, 12451−12466

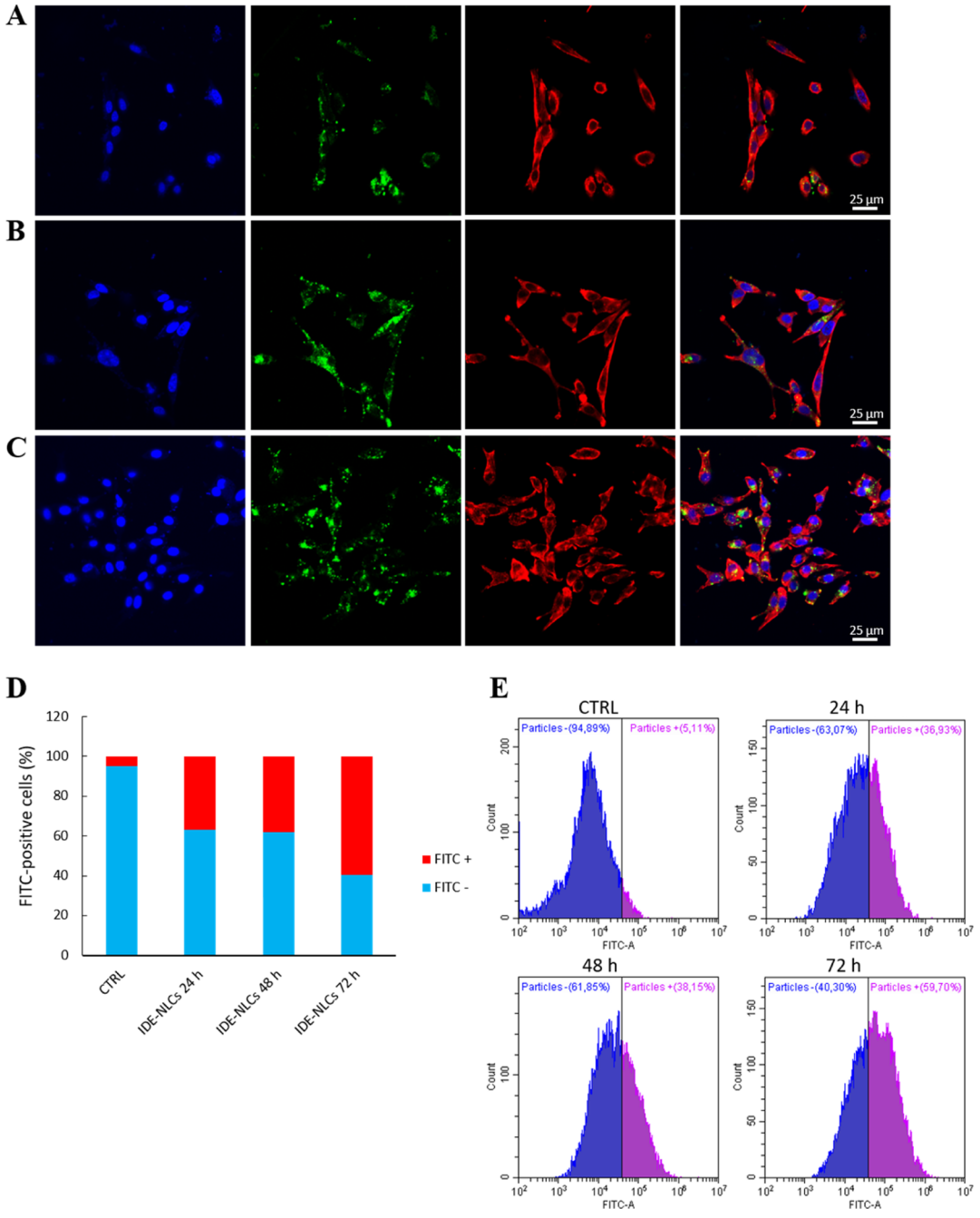

Figure 4. 2D CLSM images of C8-D1A astrocytes treated for (A) 24, (B) 48, and (C) 72 h with Vybrant DiO-labeled IDE-NLCs (green). Nuclei (blue) and f-actin (red) were also stained. (D) Flow cytometry quantification of Vybrant DiO-labeled IDE-NLCs positive cells (%) after 24, 48, and 72 h of incubation at 37 °C. (E) Representative flow cytometry plots obtained at the three time points.

incubating cells with free IDE and NLCs at the same concentrations reported above.

As shown in Figure 3A, C8-D1A cells did not exhibit any statistically significant reduction in viability at 24 h after the treatment. At 72 h, NLC formulations gave rise to a slight significant reduction of cell viability by a 20% in cells treated with IDE-NLCs and NLCs at the highest concentration ($p < 0.001$). Regarding proliferation rates, they remained unaltered at both time points (Figure S1A). In bEnd.3 cells, there were small significant effects on the viability (Figure 3B) and on cell proliferation (Figure S1B), being small fluctuations imputable to technical imprecisions. In SH-SY5Y differentiated cells, both assays showed a significant cytotoxic effect after the treatment with free IDE at the highest concentration ($p < 0.001$; Figures 3C and S1C).

Evaluation of IDE-NLC Cellular Internalization. Upon treatment with Vybrant DiO-labeled IDE-NLCs, a qualitative assessment of IDE-NLC cellular localization was performed by confocal imaging after 24 (Figures 4A, 5A, and 6A), 48 (Figures 4B, 5B, and 6B), and 72 h (Figures 4C, 5C, and 6C) of incubation. Images of the single fluorescent channels, nuclei (blue), Vybrant DiO-labeled IDE-NLCs (green), f-actin (red) were acquired. The internalization of IDE-NLCs in C8-D1A astrocytes was time-dependent, and the presence of the nanoparticles in the cytoplasm, in particular, in the perinuclear area, was detectable at 72 h after treatment (Figure 4A–C).

https://dx.doi.org/10.1021/acsomega.0c01282
ACS Omega 2020, 5, 12451−12466

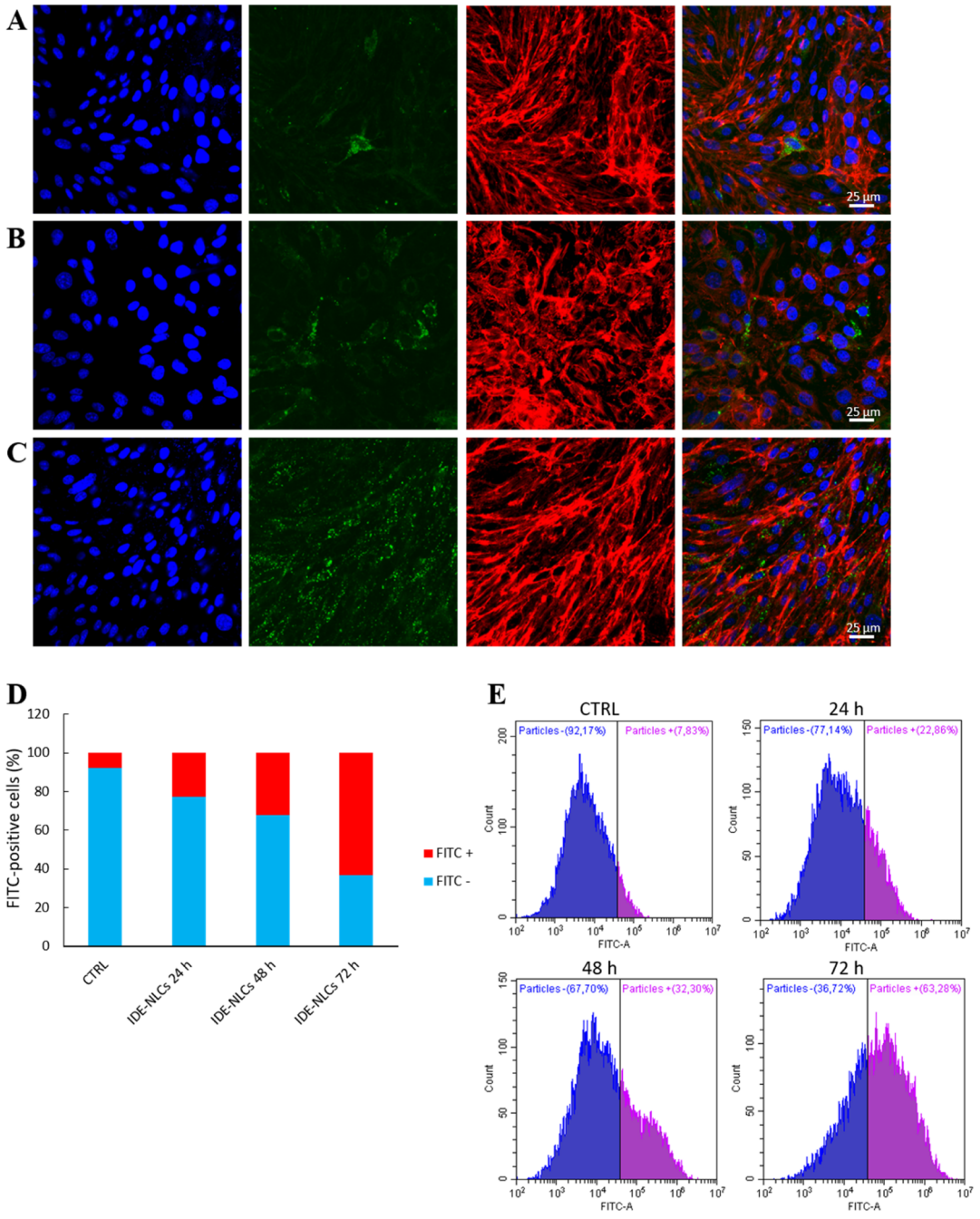

Figure 5. 2D CLSM images of bEnd.3 endothelial cells treated for (A) 24, (B) 48 and (C) 72 h with Vybrant DiO-labeled IDE-NLCs (green). Nuclei (blue) and f-actin (red) were also stained. (D) Flow cytometry quantification of Vybrant DiO-labeled IDE-NLCs positive cells (%) after 24, 48, and 72 h of incubation at 37 °C. (E) Representative flow cytometry plots obtained at the three time points.

The amount of internalized nanoparticles (Vybrant DiO-labeled IDE-NLCs) was quantified by flow cytometry, evaluating the percentage of FITC-positive cells (Figure 4D,E). These results further confirmed confocal acquisitions. The same experiment was performed on bEnd.3 cells (Figure 5A−C), which showed a predominant perinuclear localization and increased uptake of nanoparticles over time (Figure 5D,E). In differentiated neuron-like SH-SY5Y cells, IDE-NLCs uptake was clearly detectable at 48 h (Figure 6A−C), reaching 60% of FITC-positive cells at 72 h after the treatment (Figure 6D,E). Also, in this case, nanoparticles localized in the cytoplasm and, in particular, in the perinuclear area.

3D acquisitions of all the samples were performed at the three time points (Figure S2A−C).

Evaluation of the IDE-NLC Crossing Ability on an *In Vitro* BBB Model. A two-compartment model of BBB was exploited in order to evaluate IDE-NLC permeation ability. Porous scaffolds (3.0 μm diameter pores) were used for creating a separation between the two compartments where cells were cultured. In the luminal chamber (top), bEnd.3 cells were plated, while on the opposite site of the porous scaffold (abluminal compartment), C8-D1A astrocytes were grown. The BBB model displayed a TEER of 95 ± 7.5 Ω·cm^2, in agreement with other results reported in the literature.[28] FITC-dextran (70 kDa) permeability measurements are

https://dx.doi.org/10.1021/acsomega.0c01282
ACS Omega 2020, 5, 12451−12466

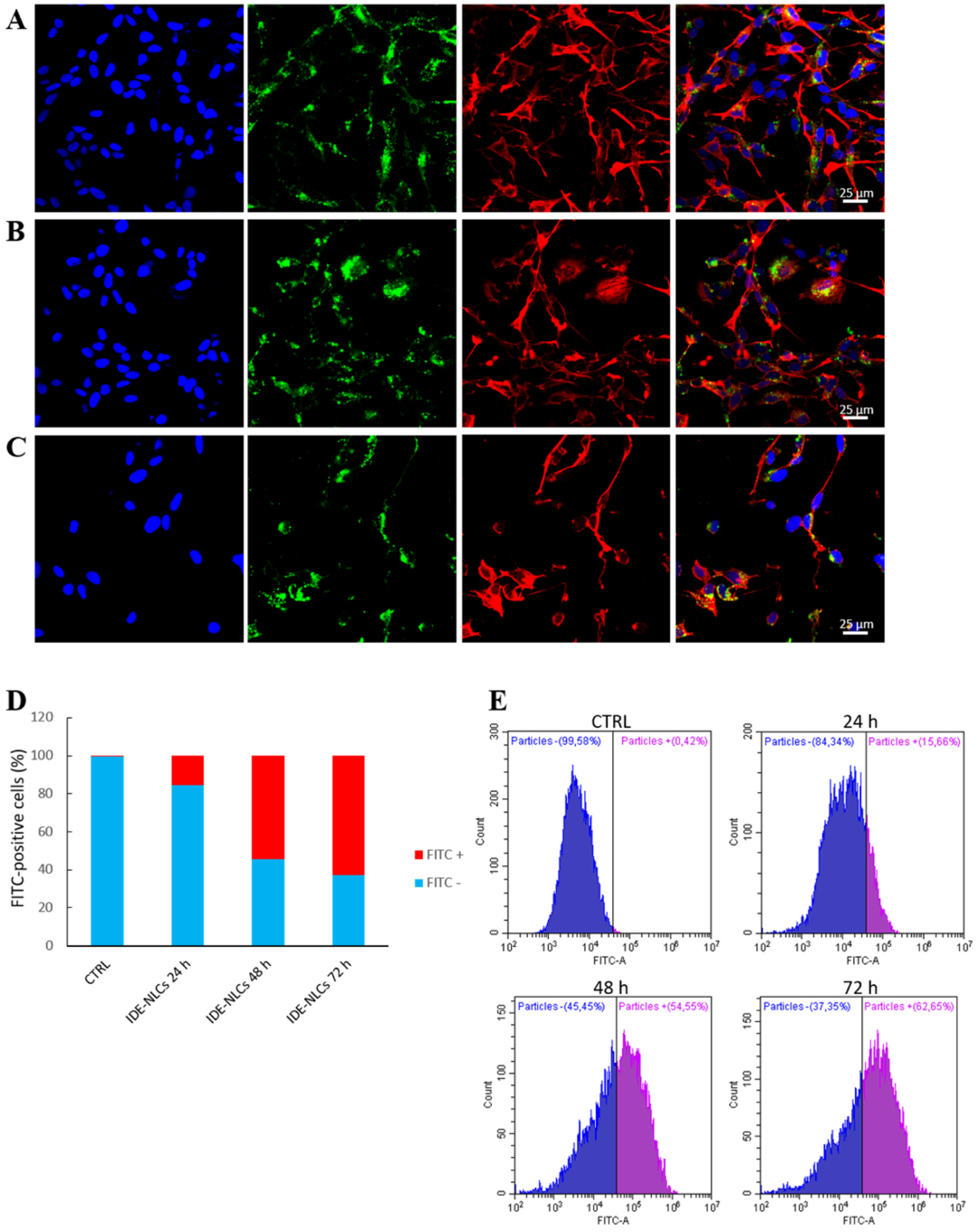

Figure 6. 2D CLSM images of differentiated SH-SY5Y neuron-like cells treated for (A) 24, (B) 48, and (C) 72 h with Vybrant DiO-labeled IDE-NLCs (green). Nuclei (blue) and f-actin (red) were also stained. (D) Flow cytometry quantification of Vybrant DiO-labeled IDE-NLCs positive cells (%) after 24, 48, and 72 h of incubation at 37 °C. (E) Representative flow cytometry plots obtained at the three time points.

reported in Figure 7A. As it can be appreciated, the FITC-dextran passage was significantly limited by the BBB with respect to the plain porous scaffold (without cells), 10.94 μg/mL *versus* 77.34 μg/mL at 72 h. In Figure 7B, the passage of Vybrant DiO-labeled IDE-NLCs through the barrier is displayed. The luminal compartment was treated with 500 μg/mL of Vybrant DiO-labeled nanoparticles, and a gradual increase in IDE-NLCs passage was appreciable, reaching 98.55 μg/mL at 72 h after incubation with cells. An increase in the amount of Vybrant DiO-labeled IDE-NLCs crossing the BBB was detectable at each time point. Representative 3D confocal images of cultured endothelial cells (Figure 7C, upper panels) and astrocytes (Figure 7C, lower panels), acquired at 72 h after incubation with Vybrant DiO-labeled IDE-NLCs (green), are reported. Nuclei (blue), f-actin (red), and merged channels were acquired. A lateral view of the *in vitro* BBB model is also shown (Figure 7C, central panels).

Evaluation of IDE-NLC Cytocompatibility in Human Healthy and ARSACS Patient's Primary Skin Fibroblasts. Cultured ARSACS patient's primary skin fibroblasts were compared to human healthy primary skin fibroblasts used as control. In order to assess the amount of metabolically active cells and their proliferation rate upon the treatment with IDE-NLCs, free IDE and NLCs, WST-1, and PicoGreen assays

https://dx.doi.org/10.1021/acsomega.0c01282
ACS Omega 2020, 5, 12451−12466

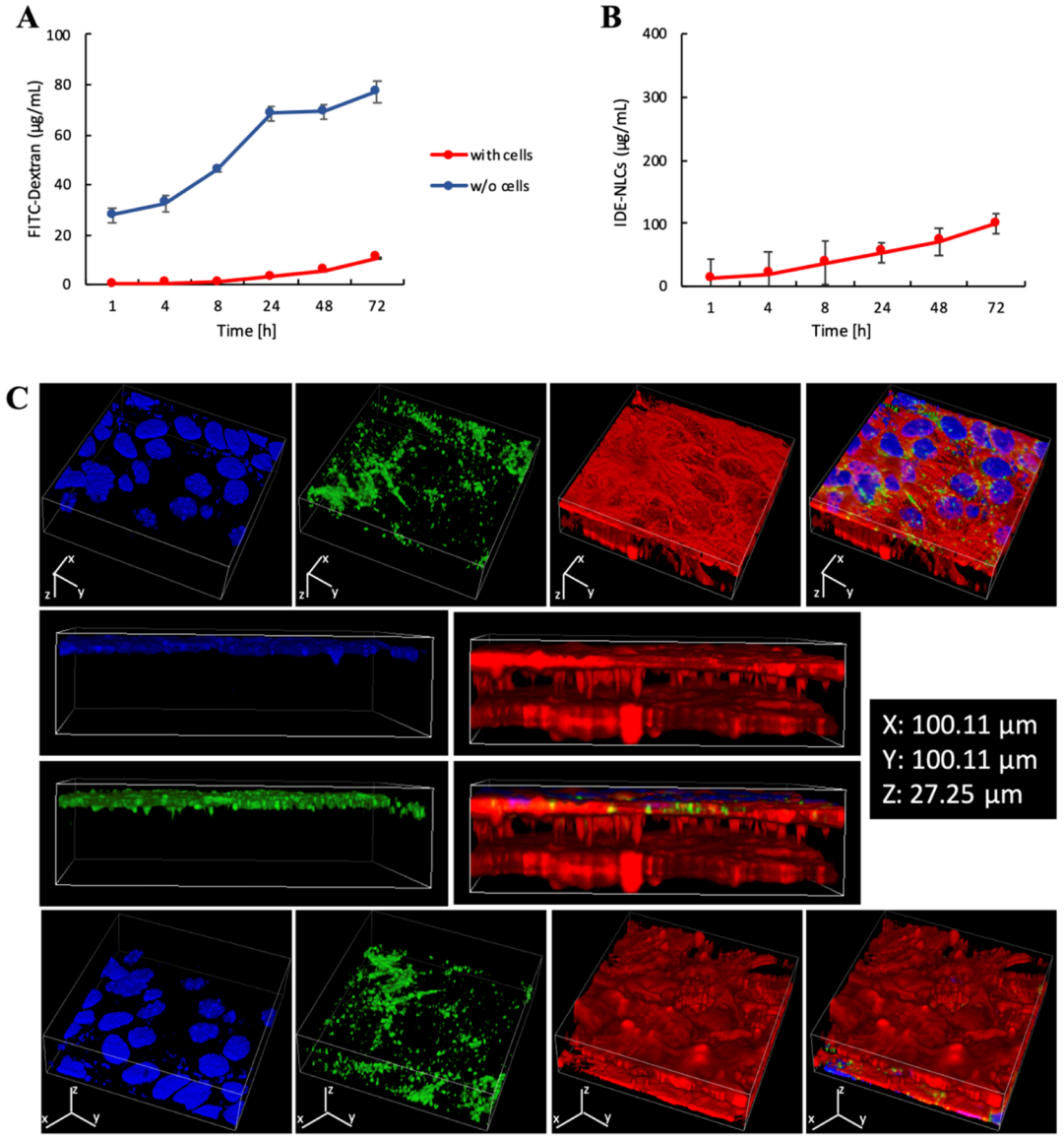

Figure 7. (A) Permeation curves of 70 kDa FITC-dextran through porous membranes with cells (red) and without cells (blue). (B) Vybrant DiO-labeled IDE-NLCs permeation curve through porous membranes with cells (red). (C) 3D CLSM images of the *in vitro* BBB model after 72 h of incubation with Vybrant DiO-labeled IDE-NLCs (green). Nuclei (blue) and f-actin (red) were also stained. In the top row, bEnd.3 cells (luminal compartment); in the bottom row, C8-D1A astrocytes (abluminal compartment); in the middle, the lateral view of the two compartments.

were performed at 24 and 72 h after administration. Figure 8A shows the results in healthy control fibroblasts incubated with IDE-NLCs, IDE, and NLCs, while Figure 8B reports the viability results obtained in treated patient's cells. As it can be seen, after the treatment with nanoparticles, healthy fibroblasts maintained their viability at both time points, even at the highest concentration of IDE-NLCs. In the case of patient's fibroblasts, cell viability was reduced by a 20% after incubation for 72 h with IDE-NLCs at the highest concentration ($p < 0.001$). Proliferation rates were also maintained in healthy fibroblasts (Figure S3A), showing slightly more variability in patient's cells (Figure S3B).

Evaluation of IDE-NLCs Cellular Internalization in Primary Skin Fibroblasts. Fibroblasts were seeded and incubated with Vybrant DiO-labeled IDE-NLCs (green) for 24 (Figures 9A and 10A), 48 (Figures 9B and 10B), and 72 h (Figures 9C and 10C), respectively, and internalization was evaluated by confocal imaging and flow cytometry. Acquired images are presented in Figure 9A−C for healthy fibroblasts and Figure 10A−C for ARSACS fibroblasts (nuclei, blue; f-actin, red; IDE-NLCs, green). The signal corresponding to the fluorescent IDE-NLCs increased between 24 and 48 h, with no significant differences between 48 and 72 h. 3D confocal images of IDE-NLC uptake were acquired of healthy (Figure S4A) and patient's (Figure S4B) fibroblasts.

The amount of internalized nanoparticles (Vybrant DiO-labeled IDE-NLCs) was quantified by flow cytometry, evaluating the percentage of FITC-positive cells. Results are reported in Figure 9D,E for human healthy fibroblasts incubated with Vybrant DiO-labeled IDE-NLCs. As it can be observed, healthy fibroblasts displayed 82% of FITC-positive cells at 24 h after administration, reaching 88% at 72 h. Results in ARSACS fibroblasts treated with Vybrant DiO-labeled IDE-NLCs showed an increase in the internalization extent between 24 and 48 h after incubation, reaching 94% of FITC-positive cells at 72 h after treatment (Figure 10D,E).

https://dx.doi.org/10.1021/acsomega.0c01282
ACS Omega 2020, 5, 12451−12466

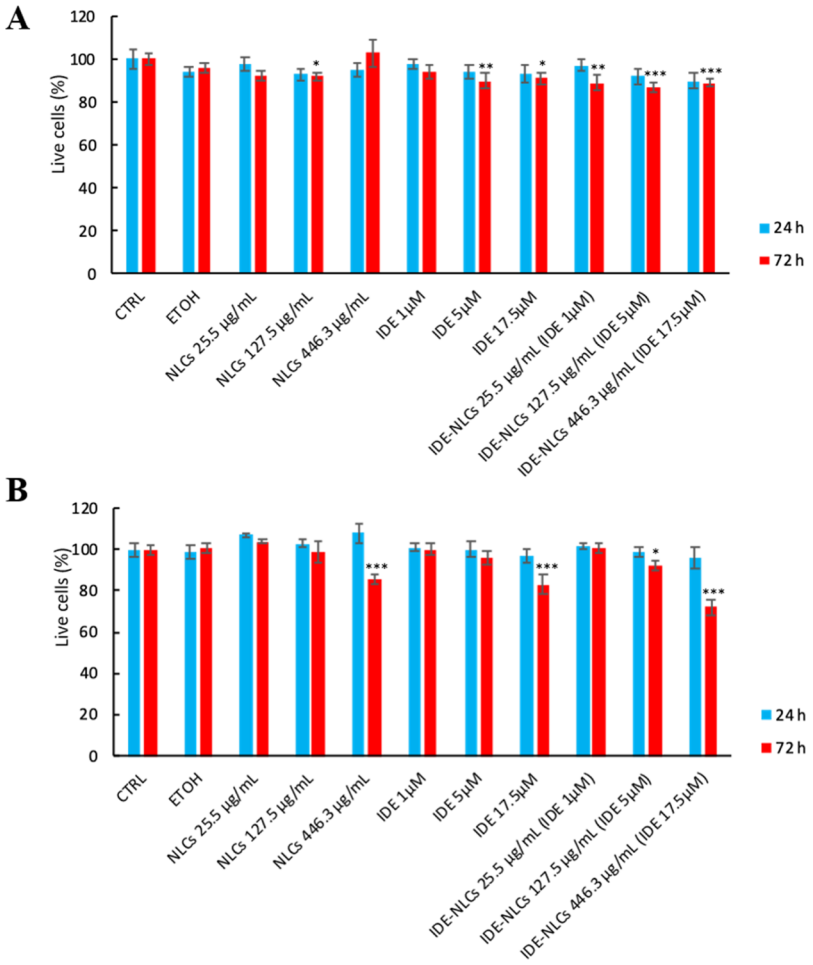

Figure 8. (A) WST-1 assay performed on human healthy primary fibroblasts incubated with free IDE, NLCs, and IDE-NLCs. (B) WST-1 assay performed on human ARSACS patient's primary fibroblasts incubated with free IDE, NLCs, and IDE-NLCs. Analyses were normalized on nontreated cells (CTRL); cells were also treated with ethanol (ETOH, used for dissolving free idebenone). *$p < 0.05$, **$p < 0.01$, ***$p < 0.001$.

Antioxidant Activity Evaluation. In order to evaluate IDE-NLCs antioxidant activity, cells were incubated with free IDE (5 μM), IDE-NLCs (300 μg/mL, corresponding to 5 μM of loaded drug), and NLCs (300 μg/mL). Analysis was conducted 72 h after incubation, staining cells with the CellRox Green Reagent. Healthy fibroblasts were treated with TBH for inducing oxidative stress. The change in the fluorescence intensity (FITC), corresponding to the ROS levels, was assessed at 30 min and 60 min after oxidative stress induction. As it can be seen in Figure 11 (upper panel), healthy fibroblasts incubated with IDE-NLCs showed reduced ROS levels, as demonstrated by the percentages of ROS-positive cells, suggestive of a protective function of IDE. In particular, control cells and NLC-treated cells showed similar percentages of ROS-positive cells (102 ± 37 and 79.5 ± 24% respectively), while cells treated with IDE and IDE-NLCs showed a statistically significant lower level ($p < 0.05$) of ROS-positive cells (5 ± 3 and 9 ± 6%, respectively). Similar results were observed in healthy fibroblasts at 60 min, with control and NLC-treated cells showing similar ROS-positive values (103 ± 40 and 60 ± 15%) and cells treated with IDE and IDE-NLCs showing statistically significant lower values ($p < 0.05$) of ROS-positive cells (8 ± 7 and 3 ± 3% respectively). The treatment with TBH caused an increment in ROS-positive cells in all experimental conditions; however, while control and NLC-treated cells showed similar ROS-positive values after the pro-oxidative stimulus at both time points (796 ± 210% for control at 30 min, 788 ± 105% for NLCs at 30 min, 1103 ± 449% for control at 60 min, and 1281 ± 331% for NLCs at 60 min), cells treated with IDE and IDE-NLCs showed statistically significant lower ($p < 0.05$) values of ROS-positive cells at 30 min (in particular 230 ± 71% for IDE and 195 ± 118% for IDE-NLCs); at 60 min, IDE-treated cells showed a statistically nonsignificant lower level of ROS-positive cells (661 ± 331%), while IDE-NLCs showed a statistically significant lower ($p < 0.05$) level of ROS-positive cells (541 ± 166%). Four experimental replicates were performed.

IDE-NLCs administered to ARSACS fibroblasts, exhibiting a higher basal level of ROS, analogously protected cells, efficiently counteracting the endogenous ROS levels, similarly to the action of free IDE (Figure 11, lower panel). In particular, control and NLC-treated cultures showed similar ROS-positive cells values at both time points (103 ± 68% for control at 30 min, 120 ± 52% for NLCs at 30 min, 92 ± 59% for control at 60 min, and 111 ± 42% for NLCs at 60 min), while IDE and IDE-NLCs treated cells showed a statistically significant ($p < 0.05$) lower level of ROS-positive cells (18 ± 2% for IDE at 30 min, 12 ± 4% for IDE-NLCs at 30 min, 12 ± 6% for IDE at 60 min, and 13 ± 5% for IDE-NLCs at 60 min). Five experimental replicates were performed. In Figure S5A, representative flow cytometry plots obtained for human healthy fibroblasts treated with free IDE, NLCs, and IDE-

https://dx.doi.org/10.1021/acsomega.0c01282
ACS Omega 2020, 5, 12451−12466

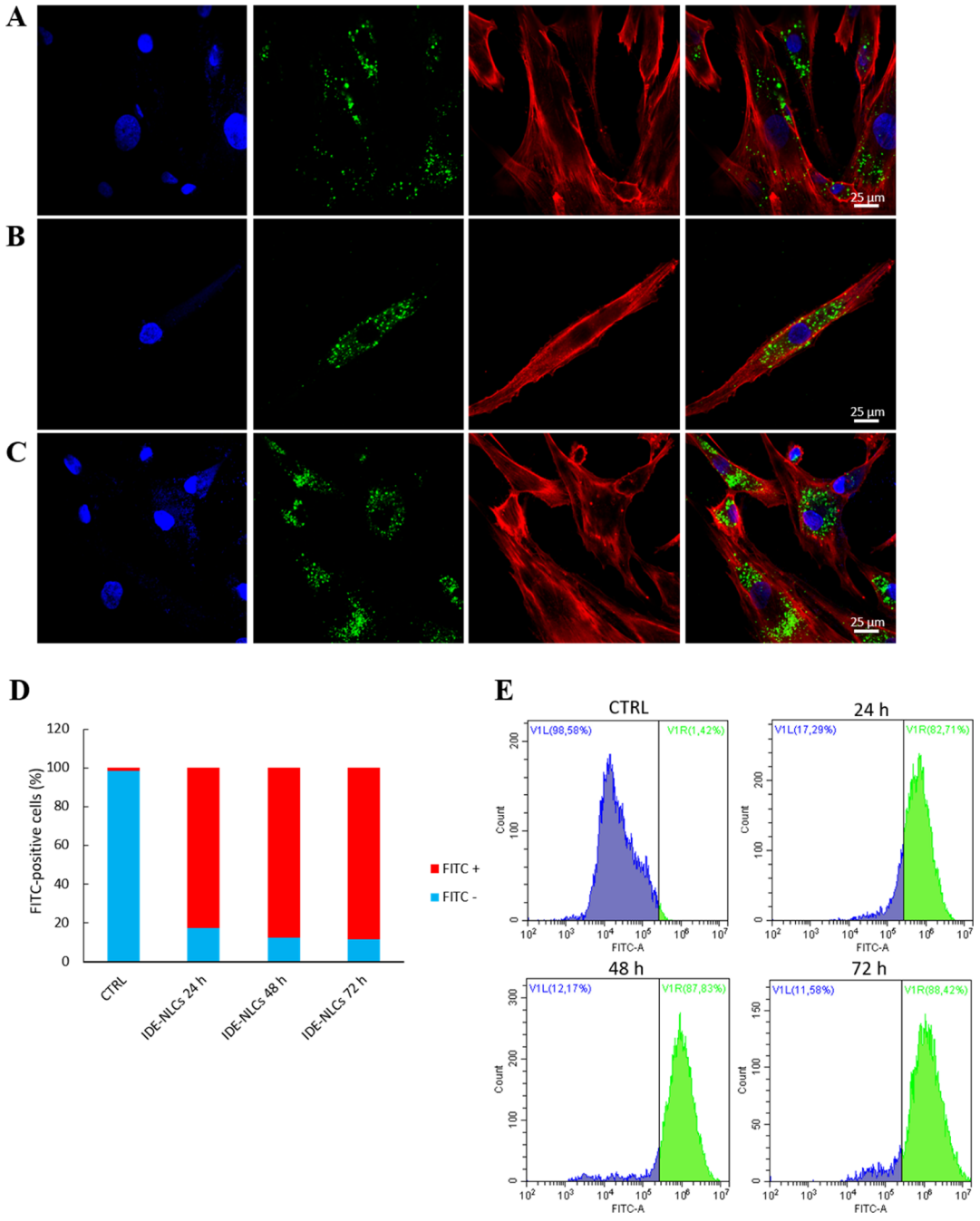

Figure 9. 2D CLSM images of human healthy primary fibroblasts treated for (A) 24, (B) 48, and (C) 72 h with Vybrant DiO-labeled IDE-NLCs (green). Nuclei (blue) and f-actin (red) were also stained. (D) Flow cytometry quantification of Vybrant DiO-labeled IDE-NLCs positive cells (%) after 24, 48, and 72 h of incubation at 37 °C. (E) Representative flow cytometry plots obtained at the three time points.

NLCs, acquired 30 and 60 min after induction of oxidative stress by TBH, are reported. Figure S5B displays representative flow cytometry plots obtained in ARSACS patient's fibroblasts treated with free IDE, NLCs, and IDE-NLCs, acquired 30 and 60 min after cell detachment.

DISCUSSION

In this work, preparation, characterization, and *in vitro* testing of NLCs encapsulating IDE for the treatment of mitochondrial pathologies have been described. More in detail, the objective of the present study was to test the significance of a novel IDE-loaded nanosystem in ARSACS, a condition were oxidative stress is constitutively high.[5] We are proposing a new strategy for future therapies exploiting biocompatible nanoparticles that are able to cross the BBB for delivering antioxidants to the cerebral compartment. The choice of the cargo has led to IDE, known for its powerful antioxidant effects, by scavenging a large variety of free radicals and by acting through electron-donor and H-donor mechanisms.[15]

NLCs were chosen for their intrinsic ability to load a large amount of payload, thanks to the liquid lipid component which forms a flawed structure. The advantages of these kinds of delivery systems are that they (i) provide prolonged drug protection, preventing fast renal clearance, (ii) they are a preferential substrate for facilitated BBB permeability because of their lipid composition, and (iii) they ensure a sustained

https://dx.doi.org/10.1021/acsomega.0c01282
ACS Omega 2020, 5, 12451−12466

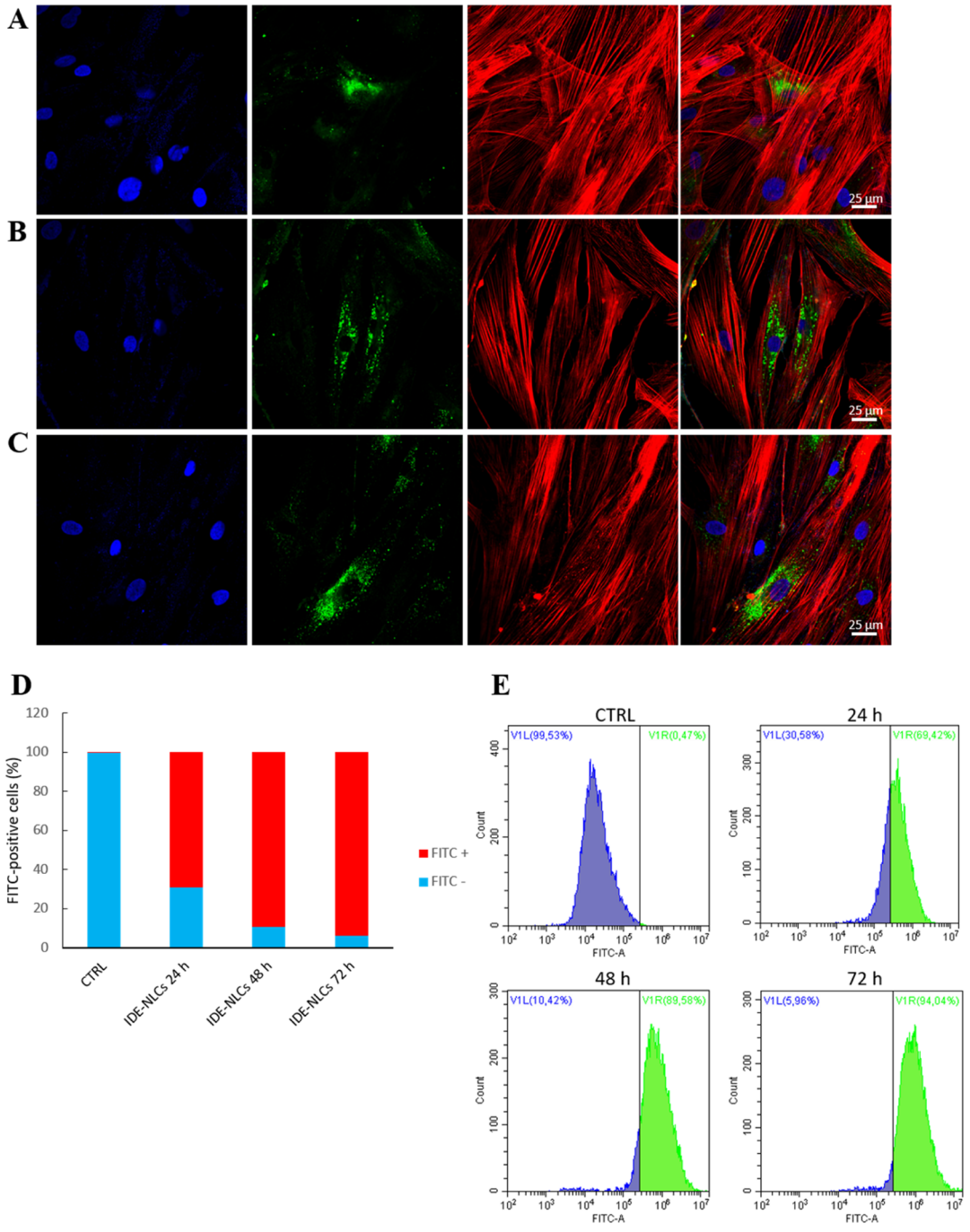

Figure 10. 2D CLSM images of human ARSACS patient's primary fibroblasts treated for (A) 24, (B) 48, and (C) 72 h with Vybrant DiO-labeled IDE-NLCs (green). Nuclei (blue) and f-actin (red) were also stained. (D) Flow cytometry quantification of Vybrant DiO-labeled IDE-NLCs positive cells (%) after 24, 48, 72 h of incubation at 37 °C. (E) Representative flow cytometry plots obtained at the three time points.

release, reducing the dose administration frequency. IDE-NLCs were fabricated by high-temperature homogenization. Although the technique and material matches are novel, the work was based on recent studies regarding brain delivery of SLNs and NLCs. Cetyl palmitate has been chosen for its ability to provide stability to nanoparticles and to impart small size and PDI, as compared to other lipids (*i.e.*, beeswax, glyceryl monostearate, and stearic acid),[29] while oleic acid was added as liquid component. IDE-NLCs showed a suitable size for nanomedical applications. Indeed, according to the literature, the best NLC size favoring BBB crossing relies approximately to 100 nm, thus avoiding fast clearance and improving drug encapsulation and delivery because of the high surface to volume ratio.[30] IDE-NLCs showed an average hydrodynamic diameter of 159.3 ± 3.4 nm, resulting small enough to discourage the obstruction of small capillaries (because of similar dimensions) and big enough to prevent blood/lymphatic system uptake.[31] Their low PDI (0.224 ± 0.015) confirmed a good homogeneity in the size and the measured ζ-potential (−33.5 ± 0.1 mV) makes NLCs highly biocompatible, attaining better colloidal stability.[32] TEM images, although different preparation methods were followed, were congruent to those reported in other works.[24,33] Regarding stability evaluation of IDE-NLCs, results demonstrated that

https://dx.doi.org/10.1021/acsomega.0c01282
ACS Omega 2020, 5, 12451−12466

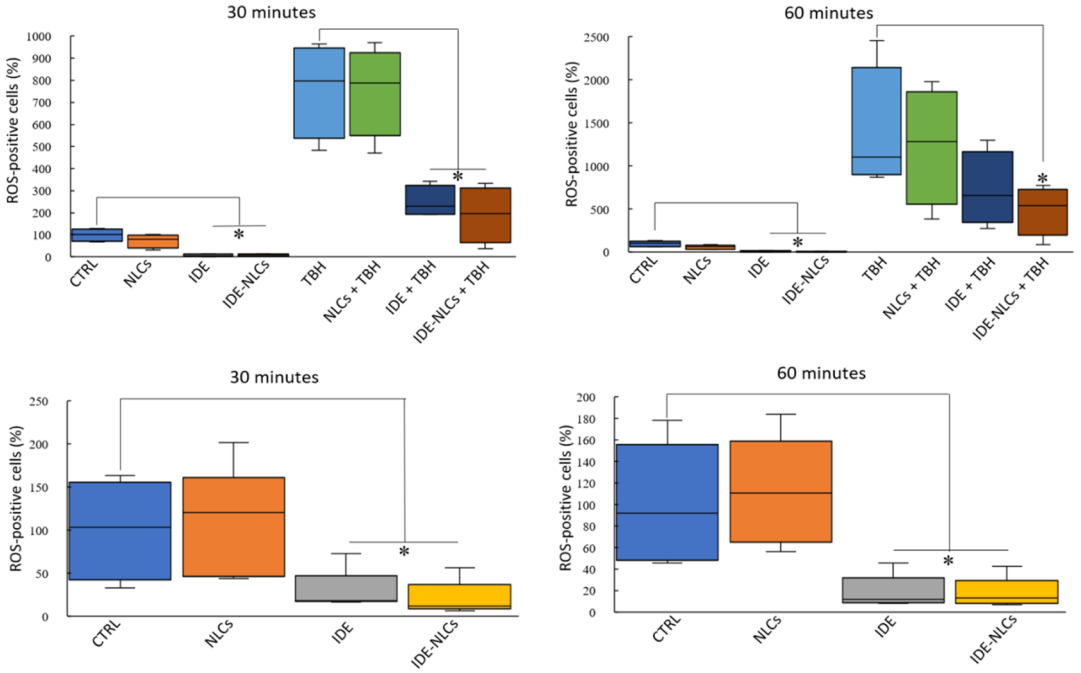

Figure 11. Upper panel: flow cytometry quantification of CellRox Green in human healthy primary fibroblasts treated with free IDE, NLCs, and IDE-NLCs for 72 h, acquired 30 min (on the left) and 60 min (on the right) after induction of oxidative stress by TBH; lower panel: flow cytometry quantification of CellRox Green in ARSACS patient's primary fibroblasts treated with free IDE, NLCs, and IDE-NLCs for 72 h, acquired 30 min (on the left) and 60 min (on the right) after cell detachment. *$p < 0.05$.

IDE-NLCs show good stability at 37 °C, even after one month and upon dilution in all the considered solvents. Furthermore, the nanovectors showed a sustained release profile reaching 13 ± 2% of IDE release at 72 h, independently from pH and redox conditions.

IDE-NLCs displayed very low cytotoxic effects, demonstrating to be biocompatible and nontoxic up to 72 h after administration in the tested cell lines. An evaluation of cytotoxicity and cell proliferation was performed on cells incubated with free drug (IDE), NLCs, and IDE-NLCs, and no significant cytotoxic effect or reduction in cell proliferation was observed, except for differentiated SH-SY5Y cells treated with the highest concentration of IDE at the longest time point. No significant differences were observed with respect to NLC and IDE-NLC treatments.

A qualitative assessment of IDE-NLC localization and internalization rates within cells was performed by confocal microscopy. The cells, maintaining a physiological cytoskeletal conformation, presented a cytoplasm rich in nanoparticles, with a time-dependent internalization (mostly after 48 h of treatment), mainly localized in the perinuclear area for all the analyzed cell lines. A quantitative assessment of IDE-NLC internalization was then conducted by flow cytometry. Also, in this case, the internalization was mostly time-dependent, reaching a good amount of nanoparticles in the cells after 72 h in all the cell lines analyzed. Regarding their ability to cross BBB, an *in vitro* model resembling the endothelial monolayer (top, luminal compartment) and the astrocytes (bottom, abluminal compartment) was exploited, resulting in a TEER of 95 ± 7.5 $\Omega \cdot cm^2$. IDE-NLCs were able to permeate the BBB model and settled the crossing percentage at 19.71% after 72 h. These preliminary data seem to be very promising and indicate the capacity of the nanoparticles to cross an *in vitro* model of BBB, further corroborating their possible evaluation for future *in vivo* studies.

Promising results have been obtained for the evaluation of IDE-NLC antioxidant efficacy. IDE-NLCs showed an effective antioxidant protection on human healthy primary skin fibroblasts. Further studies will be required in order to better evaluate the efficacy of loaded nanoparticles, considering also the possible variations in the patient's responses to increased oxidative stress.

Because mitochondrial dysfunctions characterize many neurodegenerative conditions, in the last years new therapeutic strategies have been envisaged. Mitochondrial targeting could be a straightforward method for delivering IDE to the site of interest. In fact, one of the limitations of antioxidants is their inability to function within the mitochondria.[34] It has been shown that lipophilic cations selectively accumulate within the mitochondria, because of their negative membrane potential (130/150 mV in living cells).[35] Indeed, they are used to measure mitochondrial membrane potential (*e.g.*, triphenylmethylphosphonium, TPP) as well as to localize the mitochondria by fluorescence microscopy (*e.g.*, rhodamine). It has been demonstrated that by conjugating TPP^+ salt with the antioxidant phenolic moiety of vitamin E (MitoVitE), this was efficiently delivered to the mitochondria. The amount of MitoVitE specifically uptaken was approximately 80-fold higher than the endogenous levels of vitamin E.[36] Furthermore, it has been shown that MitoVitE was 800-fold more potent than IDE in cultured fibroblasts derived from patients affected by FA.[37] A similar approach could be applied to IDE, in order to improve its function once released from NLCs.

■ CONCLUSIONS

To summarize, biocompatible nanoparticles have been developed as an effective antioxidant delivery system not only for the treatment of mitochondrial pathologies, yet also as a novel therapeutic approach for ARSACS and, more in

https://dx.doi.org/10.1021/acsomega.0c01282
ACS Omega 2020, 5, 12451−12466

general, for neurodegeneration. In order to make these nanovectors applicable for the treatment of mitochondrial dysfunctions characterizing many NDs, future IDE-NLCs could be functionalized with a signal peptide, allowing their attachment to any mitochondrial subunit and leading to their targeted import.

■ ASSOCIATED CONTENT

Supporting Information

The Supporting Information is available free of charge at https://pubs.acs.org/doi/10.1021/acsomega.0c01282.

PicoGreen assay on C8-D1A, bEnd.3, and SH-SY5Y cell lines; 3D CLSM rendering of C8-D1A, bEnd.3, and SH-SY5Y cell lines; PicoGreen assay on human healthy primary and ARSACS patient's primary fibroblasts; 3D CLSM rendering of human healthy primary and ARSACS patient's primary fibroblasts; and representative flow cytometry plots for human healthy primary and ARSACS patient's primary fibroblasts (PDF)

■ AUTHOR INFORMATION

Corresponding Authors

Chiara Martinelli − *Smart Bio-Interfaces, Istituto Italiano di Tecnologia, 56025 Pontedera, Italy*; Email: chiara.martinelli@iit.it

Gianni Ciofani − *Smart Bio-Interfaces, Istituto Italiano di Tecnologia, 56025 Pontedera, Italy*; orcid.org/0000-0003-1192-3647; Email: gianni.ciofani@iit.it

Authors

Matteo Battaglini − *Smart Bio-Interfaces, Istituto Italiano di Tecnologia, 56025 Pontedera, Italy; The Biorobotics Institute, Scuola Superiore Sant'Anna, 56025 Pontedera, Italy*

Carlotta Pucci − *Smart Bio-Interfaces, Istituto Italiano di Tecnologia, 56025 Pontedera, Italy*

Sara Gioi − *Department of Mechanical and Aerospace Engineering, Politecnico di Torino, 10129 Torino, Italy*

Chiara Caracci − *Department of Mechanical and Aerospace Engineering, Politecnico di Torino, 10129 Torino, Italy*

Gaia Macaluso − *Dipartimento di Biologia, Università di Pisa, 56126 Pisa, Italy*

Stefano Doccini − *Molecular Medicine for Neurodegenerative and Neuromuscular Diseases Unit, IRCCS Fondazione Stella Maris, 56128 Pisa, Italy*

Filippo M. Santorelli − *Molecular Medicine for Neurodegenerative and Neuromuscular Diseases Unit, IRCCS Fondazione Stella Maris, 56128 Pisa, Italy*

Complete contact information is available at: https://pubs.acs.org/10.1021/acsomega.0c01282

Author Contributions

The manuscript was written through contributions of all authors. All authors have given approval to the final version of the manuscript.

Funding

This research was supported by the Italian Ministry of Health (grant no. RF-2016-02361610).

Notes

The authors declare no competing financial interest.

■ ACKNOWLEDGMENTS

The authors would like to thank Dr. Doriana Debellis and Dr. Rosaria Brescia (Istituto Italiano di Tecnologia, Italy) for TEM imaging support, and Dr. Christos Tapeinos and Dr. Attilio Marino (Istituto Italiano di Tecnologia, Italy) for support in materials synthesis and *in vitro* models, respectively.

■ ABBREVIATIONS

APPH, 2,2-azobis 2-amidopropane dihydrochloride; ARSACS, autosomal recessive spastic ataxia of Charlevoix-Saguenay; BBB, blood−brain barrier; CLSM, confocal laser scanning microscopy; DLS, dynamic light scattering; FA, Friedreich's ataxia; FBS, fetal bovine serum; HPLC, high-performance liquid chromatography; IDE, idebenone; LDH, lower induced release of lactate dehydrogenase; NDs, neurodegenerative diseases; NLCs, nanostructured lipid carriers; PDI, polydispersity index; ROS, reactive oxygen species; *SACS*, sacsin gene; SLNs, solid lipid nanoparticles; TBH, *tert*-butyl hydroperoxide; TEM, transmission electron microscopy; TPP, triphenylmethylphosphonium

■ REFERENCES

(1) Jellinger, K. A. Basic Mechanisms of Neurodegeneration: A Critical Update. *J. Cell. Mol. Med.* **2010**, *14*, 457−487.

(2) Barnham, K. J.; Masters, C. L.; Bush, A. I. Neurodegenerative Diseases and Oxidatives Stress. *Nat. Rev. Drug Discovery* **2004**, *3*, 205−214.

(3) Gandhi, S.; Abramov, A. Y. Mechanism of Oxidative Stress in Neurodegeneration. *Oxid. Med. Cell. Longevity* **2012**, *2012*, 428010.

(4) Martinelli, C.; Pucci, C.; Battaglini, M.; Marino, A.; Ciofani, G. Antioxidants and Nanotechnology: Promises and Limits of Potentially Disruptive Approaches in the Treatment of Central Nervous System Diseases. *Adv. Healthcare Mater.* **2020**, *9*, 1901589.

(5) Engert, J. C.; Bérubé, P.; Mercier, J.; Doré, C.; Lepage, P.; Ge, B.; Bouchard, J.-P.; Mathieu, J.; Melançon, S. B.; Schalling, M.; Lander, E. S.; Morgan, K.; Hudson, T. J.; Richter, A. ARSACS, a Spastic Ataxia Common in Northeastern Quebec, Is Caused by Mutations in a New Gene Encoding an 11.5-Kb ORF. *Nat. Genet.* **2000**, *24*, 120−125.

(6) Criscuolo, C.; Procaccini, C.; Meschini, M. C.; Cianflone, A.; Carbone, R.; Doccini, S.; Devos, D.; Nesti, C.; Vuillaume, I.; Pellegrino, M.; Filla, A.; De Michele, G.; Matarese, G.; Santorelli, F. M. Powerhouse Failure and Oxidative Damage in Autosomal Recessive Spastic Ataxia of Charlevoix-Saguenay. *J. Neurol.* **2015**, *262*, 2755−2763.

(7) Girard, M.; Lariviere, R.; Parfitt, D. A.; Deane, E. C.; Gaudet, R.; Nossova, N.; Blondeau, F.; Prenosil, G.; Vermeulen, E. G. M.; Duchen, M. R.; Richter, A.; Shoubridge, E. A.; Gehring, K.; McKinney, R. A.; Brais, B.; Chapple, J. P.; McPherson, P. S. Mitochondrial Dysfunction and Purkinje Cell Loss in Autosomal Recessive Spastic Ataxia of Charlevoix-Saguenay (ARSACS). *Proc. Natl. Acad. Sci. U.S.A.* **2012**, *109*, 1661−1666.

(8) Ricca, I.; Morani, F.; Bacci, G. M.; Nesti, C.; Caputo, R.; Tessa, A.; Santorelli, F. M. Clinical and Molecular Studies in Two New Cases of ARSACS. *Neurogenetics* **2019**, *20*, 45−49.

(9) Pilliod, J.; Moutton, S.; Lavie, J.; Maurat, E.; Hubert, C.; Bellance, N.; Anheim, M.; Forlani, S.; Mochel, F.; N'Guyen, K.; Thauvin-Robinet, C.; Verny, C.; Milea, D.; Lesca, G.; Koenig, M.; Rodriguez, D.; Houcinat, N.; Van-Gils, J.; Durand, C. M.; Guichet, A.; Barth, M.; Bonneau, D.; Convers, P.; Maillart, E.; Guyant-Marechal, L.; Hannequin, D.; Fromager, G.; Afenjar, A.; Chantot-Bastaraud, S.; Valence, S.; Charles, P.; Berquin, P.; Rooryck, C.; Bouron, J.; Brice, A.; Lacombe, D.; Rossignol, R.; Stevanin, G.; Benard, G.; Burglen, L.; Durr, A.; Goizet, C.; Coupry, I. New Practical Definitions for the Diagnosis of Autosomal Recessive Spastic Ataxia of Charlevoix-Saguenay. *Ann. Neurol.* **2015**, *78*, 871−886.

(10) Sferra, A.; Fattori, F.; Rizza, T.; Flex, E.; Bellacchio, E.; Bruselles, A.; Petrini, S.; Cecchetti, S.; Teson, M.; Restaldi, F.; Ciolfi, A.; Santorelli, F. M.; Zanni, G.; Barresi, S.; Castiglioni, C.; Tartaglia, M.; Bertini, E. Defective Kinesin Binding of TUBB2A Causes Progressive Spastic Ataxia Syndrome Resembling Sacsinopathy. *Hum. Mol. Genet.* **2018**, *27*, 1892−1904.
(11) Cipolla, M. J. The Cerebral Circulation. *Control Of Cerebral Blood Flow*; Morgan & Claypool Life Sciences: San Rafael (CA), 2009; Chapter 5.
(12) Martinelli, C.; Pucci, C.; Ciofani, G. Nanostructured Carriers as Innovative Tools for Cancer Diagnosis and Therapy. *APL Bioeng.* **2019**, *3*, 011502.
(13) Tapeinos, C.; Battaglini, M.; Ciofani, G. Advances in the Design of Solid Lipid Nanoparticles and Nanostructured Lipid Carriers for Targeting Brain Diseases. *J. Controlled Release* **2017**, *264*, 306−332.
(14) Jaber, S.; Polster, B. M. Idebenone and Neuroprotection: Antioxidant, pro-Oxidant, or Electron Carrier? *J. Bioenerg. Biomembr.* **2015**, *47*, 111−118.
(15) Mordente, A.; Martorana, G. E.; Minotti, G.; Giardina, B. Antioxidant Properties of 2,3-Dimethoxy-5-Methyl-6-(10-Hydroxydecyl)- 1,4-Benzoquinone (Idebenone). *Chem. Res. Toxicol.* **1998**, *11*, 54−63.
(16) Montenegro, L.; Turnaturi, R.; Parenti, C.; Pasquinucci, L. Idebenone: Novel Strategies to Improve Its Systemic and Local Efficacy. *Nanomaterials* **2018**, *8*, 87.
(17) Carelli, V.; Carbonelli, M.; De Coo, I. F.; Kawasaki, A.; Klopstock, T.; Lagrèze, W. A.; La Morgia, C.; Newman, N. J.; Orssaud, C.; Pott, J. W. R.; Sadun, A. A.; van Everdingen, J.; Vignal-Clermont, C.; Votruba, M.; Yu-Wai-Man, P.; Barboni, P. International Consensus Statement on the Clinical and Therapeutic Management of Leber Hereditary Optic Neuropathy. *J. Neuro Ophthalmol.* **2017**, *37*, 371−381.
(18) Lyseng-Williamson, K. A. Idebenone: A Review in Leber's Hereditary Optic Neuropathy. *Drugs* **2016**, *76*, 805−813.
(19) Montenegro, L.; Sinico, C.; Castangia, I.; Carbone, C.; Puglisi, G. Idebenone-Loaded Solid Lipid Nanoparticles for Drug Delivery to the Skin: In Vitro Evaluation. *Int. J. Pharm.* **2012**, *434*, 169−174.
(20) Muscoli, C.; Fresta, M.; Cardile, V.; Palumbo, M.; Renis, M.; Puglisi, G.; Paolino, D.; Nisticò, S.; Rotiroti, D.; Mollace, V. Ethanol-Induced Injury in Rat Primary Cortical Astrocytes Involves Oxidative Stress: Effect of Idebenone. *Neurosci. Lett.* **2002**, *329*, 21−24.
(21) Paolino, D.; Iannone, M.; Cardile, V.; Renis, M.; Puglisi, G.; Rotiroti, D.; Fresta, M. Tolerability and Improved Protective Action of Idebenone-Loaded Pegylated Liposomes on Ethanol-Induced Injury in Primary Cortical Astrocytes. *J. Pharm. Sci.* **2004**, *93*, 1815−1827.
(22) Stancampiano, A. H. S.; Acquaviva, R.; Campisi, A.; Vanella, L.; Ventura, C. A.; Puglisi, G.; Pignatello, R. Technological and Biological Characterization of Idebenone-Loaded Solid Lipid Nanoparticles Prepared by a Modified Solvent Injection Technique. *J. Biomed. Nanotechnol.* **2006**, *2*, 253−270.
(23) Montenegro, L.; Campisi, A.; Sarpietro, M. G.; Carbone, C.; Acquaviva, R.; Raciti, G.; Puglisi, G. In Vitro Evaluation of Idebenone-Loaded Solid Lipid Nanoparticles for Drug Delivery to the Brain. *Drug Dev. Ind. Pharm.* **2011**, *37*, 737−746.
(24) Montenegro, L.; Trapani, A.; Latrofa, A.; Puglisi, G. In Vitro Evaluation on a Model of Blood Brain Barrier of Idebenone-Loaded Solid Lipid Nanoparticles. *J. Nanosci. Nanotechnol.* **2012**, *12*, 330−337.
(25) Battaglini, M.; Tapeinos, C.; Cavaliere, I.; Marino, A.; Ancona, A.; Garino, N.; Cauda, V.; Palazon, F.; Debellis, D.; Ciofani, G. Design, fabrication, and in vitro evaluation of nanoceria-loaded nanostructured lipid carriers for the treatment of neurological diseases. *ACS Biomater. Sci. Eng.* **2019**, *5*, 670−682.
(26) Dwane, S.; Durack, E.; Kiely, P. A. Optimising parameters for the differentiation of SH-SY5Y cells to study cell adhesion and cell migration. *BMC Res. Notes* **2013**, *6*, 366.
(27) Wolff, A.; Antfolk, M.; Brodin, B.; Tenje, M. In Vitro Blood-Brain Barrier Models-An Overview of Established Models and New Microfluidic Approaches. *J. Pharm. Sci.* **2015**, *104*, 2727−2746.
(28) Helms, H. C.; Abbott, N. J.; Burek, M.; Cecchelli, R.; Couraud, P.-O.; Deli, M. A.; Förster, C.; Galla, H. J.; Romero, I. A.; Shusta, E. V.; Stebbins, M. J.; Vandenhaute, E.; Weksler, B.; Brodin, B. In Vitro Models of the Blood-Brain Barrier: An Overview of Commonly Used Brain Endothelial Cell Culture Models and Guidelines for Their Use. *J. Cereb. Blood Flow Metab.* **2016**, *36*, 862−890.
(29) Jenning, V.; Gohla, S. Comparison of Wax and Glyceride Solid Lipid Nanoparticles (SLN). *Int. J. Pharm.* **2000**, *196*, 219−222.
(30) Rizvi, S. A. A.; Saleh, A. M. Applications of Nanoparticle Systems in Drug Delivery Technology. *Saudi Pharm. J.* **2018**, *26*, 64−70.
(31) Prokop, A.; Davidson, J. M. Nanovehicular Intracellular Delivery Systems. *J. Pharm. Sci.* **2008**, *97*, 3518−3590.
(32) Peer, D.; Karp, J. M.; Hong, S.; Farokhzad, O. C.; Margalit, R.; Langer, R. Nanocarriers as an Emerging Platform for Cancer Therapy. *Nat. Nanotechnol.* **2007**, *2*, 751−760.
(33) Mandpe, L.; Kyadarkunte, A.; Pokharkar, V. Assessment of Novel Iloperidone-and Idebenone-Loaded Nanostructured Lipid Carriers: Brain Targeting Efficiency and Neuroprotective Potential. *Ther. Delivery* **2013**, *4*, 1365−1383.
(34) Moreira, P. I.; Zhu, X.; Wang, X.; Lee, H.-g.; Nunomura, A.; Petersen, R. B.; Perry, G.; Smith, M. A. Mitochondria: A Therapeutic Target in Neurodegeneration. *Biochim. Biophys. Acta* **2010**, *1802*, 212−220.
(35) Murphy, M. P.; Smith, R. A. J. Drug Delivery to Mitochondria: The Key to Mitochondrial Medicine. *Adv. Drug Delivery Rev.* **2000**, *41*, 235−250.
(36) Smith, R. A. J.; Porteous, C. M.; Coulter, C. V.; Murphy, M. P. Selective Targeting of an Antioxidant to Mitochondria. *Eur. J. Biochem.* **1999**, *263*, 709−716.
(37) Jauslin, M. L.; Meier, T.; Smith, R. A. J.; Murphy, P. M. Mitochondria-Targeted Antioxidants Protect Friedreich Ataxia Fibroblasts from Endogenous Oxidative Stress More Effectively than Untargeted Antioxidants. *FASEB J.* **2003**, *17*, 1−10.

https://dx.doi.org/10.1021/acsomega.0c01282
ACS Omega 2020, 5, 12451−12466